ANALYSIS OF VOLTS PER HERTZ SCALAR CONTROL AS GOVERNOR OF HIGH POLE COUNT, HIGH FREQUENCY, PERMANENT MAGNET SYNCHRONOUS MACHINE

BY

KATHERINE M. O'KANE

THESIS

Submitted in partial fulfillment of the requirements
for the degree of Master of Science in Electrical and Computer Engineering
in the Graduate College of the
University of Illinois at Urbana-Champaign, 2017

Urbana, Illinois

Adviser:

Associate Professor Kiruba Sivasubramaniam Haran

ABSTRACT

This thesis focuses on the volts per hertz control architecture developed by the Haran Research team at the University of Illinois at Urbana-Champaign to control a 1 MW permanent magnet synchronous machine (PMSM) intended to propel a hybrid-electric commercial aircraft. At the time of this writing, the first iteration of the NASA PMSM high pole count, low impedance, high power motor is being constructed. This motor is capable of high rotational speeds and features a unique flying capacitor multi-level (FCML) inverter system.

First, an overview of the development of a volts per hertz controller is reviewed followed by implementation of the controller in Simulink. As the system design has inherent oscillations, a PD control is developed for the system as well as a ramping function to keep machine speed and electrical frequency aligned as well as limit torque output. The design of the system control is followed by an analysis of the control implications, namely, system dynamic performance; comparison to an alternative control strategy, field oriented control (FOC); and comparison of the motor control dynamics with that of modern combustion propulsion systems.

To my family and friends.
A million thanks for your unwavering love, encouragement, and support.

ACKNOWLEDGMENTS

My adviser
KIRUBA SIVASUBRAMANIAM HARAN, PH.D., P.E.
for his academic expertise, advice, and support as well as the entire
HARAN RESEARCH GROUP.

Our research sponsors, the
NATIONAL AERONAUTICS AND SPACE ADMINISTRATION (NASA)
and
THE GRAINGER CENTER FOR
ELECTRIC MACHINERY AND ELECTROMECHANICS.

The Senior Design Project Laboratory staff of Fall 2015, 2016, particularly,
P. SCOTT CARNEY, PH.D and JONATHAN J. MAKELA, PH.D
for the opportunity to teach and learn all at once.

The Department of Electrical and Computer Engineering at
THE UNIVERSITY OF ILLINOIS AT URBANA-CHAMPAIGN
for the astounding resources and collective knowledge as well as the
financial support that made my graduate education possible.

My parents
JAMES C. O'KANE and LEIGH A. BROCONE
for being the lifelong champions of my success.

My sister
SHANNEN M. O'KANE
for being my best friend and driving me to be a role model.

TABLE OF CONTENTS

CHAPTER 1

INTRODUCTION

1.1 High Power Density Permanent Magnet Synchronous Machine Project

This project is part of the development of a permanent magnet synchronous machine (PMSM) intended for eventual use as a propulsor within commercial aircraft funded by the National Aeronautics and Space Administration (NASA) under Grant NNX14AL79A purposed for Space Science and Applications - Basic Research. At the University of Illinois at Urbana-Champaign, this effort is being led by Dr. Kirbua Sivasubramaniam Haran, focusing on the motor design and high level motor control, and Dr. Robert Pilawa-Podgurski, focusing on design of the power electronics and low level control of the inverters. Current research by the team has been related to the development of the external rotor, high specific power, and high flux density PMSM rated for a speed of 15 krpm and 1 MW; the electric drive flying-capacitor multi-level (FCML) inverter architecture; and the corresponding controls to govern the aforementioned physical components. Information on the inverter architecture can be found in [1], and the design for the external rotor, air cooled PMSM is shown in Figure 1.1.

The current electronic control architecture of the system includes an array of field programmable gate arrays (FPGAs) that will control the gate signals to each of the cascaded FCMLs needed for each phase of the PMSM and a governing microcontroller (MCU) that will process feedback, control the PMSM's rotation under varying torque load, and communicate control commands to the FPGAs. A depiction of the system architecture can be seen in Figure 1.2. The focus of this thesis will be on the design and simulation of a supervisory control scheme to be uploaded on the MCU: volts per hertz control (V/f).

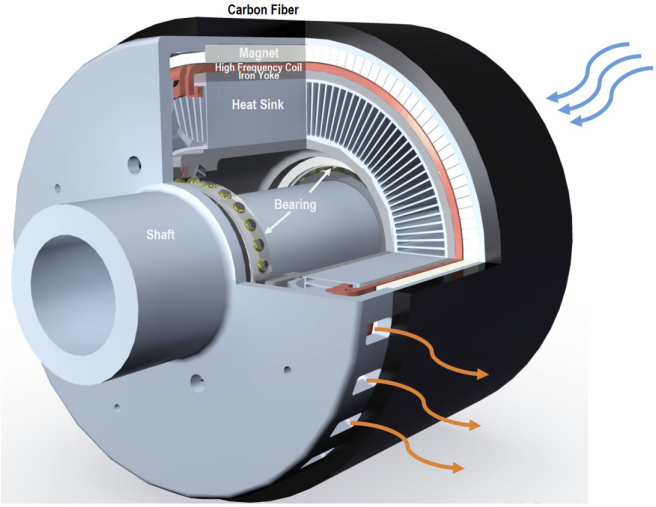

Figure 1.1: 1 MW High Power Density Permanent Magnet Synchronous Machine [2]

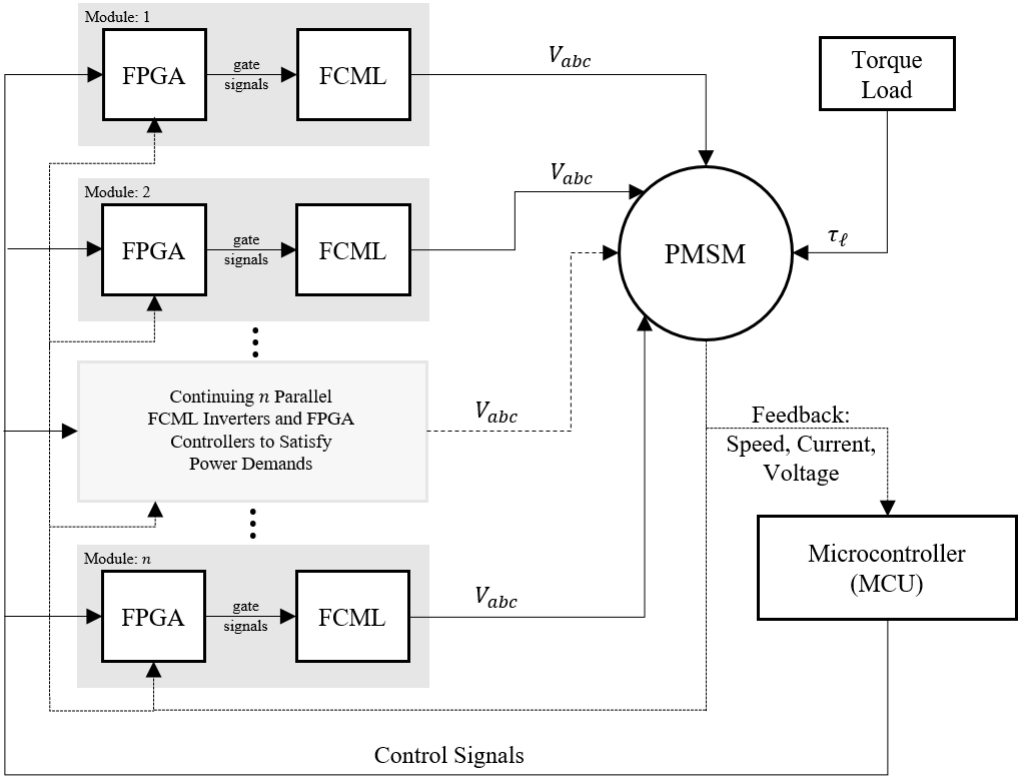

Figure 1.2: Proposed Electronic Hardware and Data Transfer Layout

1.2 Control Research Motivation

The selection of volts per hertz control for this study as opposed to field oriented control (FOC) — another standard control scheme for the PMSM that controls the current vectors in the torque, d, and flux, q, axis (also called the dq-axis) and, through a transformation, computes the desired phase voltages — is to explore a simpler control structure that will require smaller computational density by decreasing the number of preliminary calculations before a control effort is found. For vector control, the additional overhead of the flux reference calculation, Clarke transform, Park transform, inverse Park transform, and inverse Clarke transform are added to the control computations [3]. Though vector control of a high speed PMSM has been accomplished, as in [4], the high power of this system, causing a substantially increased number of signals associated with cascaded FCMLs, as was shown in Figure 1.2, produces additional system failure modes with each additional computation. For instance, in experiments done previous to this work, it was found that inaccuracy in torque and flux estimation calculations used to find rotor position could cause the rotor to fail to start. Additionally, position sensors, required for FOC control but not in V/f, introduce another feedback signal that is subject to measurement and mechanical failures. Additionally, literary studies focused on high speed applications of PMSMs have consistently concluded that for high speed applications, volts per hertz control is the control scheme of choice [5], [6].

Though volts per hertz has been commonly found in high speed applications, the NASA PMSM is decidedly a mid-speed motor in comparison to these works, so no conclusion about this particular speed range has been definitively made at this time. Furthermore, the system dynamics for a high speed, low impedance, high pole count PMSM are also of special interest as high speed machines studied in the past commonly have larger stator impedances and fewer poles, so the performance of the NASA PMSM is not well known [5]-[7]. Because of the uncertainty of which model will work better for system performance, studies have been done on both control system designs, with FOC studies performed by another member of the research team, Xiaolong Zhang, with an intent to compare the performance of the two control models and conclude which is more appropriate for the application.

CHAPTER 2

OVERVIEW OF THE DESIGN PROCESS FOR PMSM SCALAR CONTROL

2.1 Mathematical Model for the PMSM Volts per Hertz Controller

To obtain an understanding of the volts per hertz control structure, it is necessary to study the system dynamics of PMSMs and create a model for the system so that it can be controlled. As this time, the circuit model and electrical analysis for the PMSM have been covered in a number of texts, so a brief discussion of the content will be presented here based on the work described in [3] and [7]. For the NASA motor, the back emf waveform is sinusoidal, as is typical for high performance applications, and the windings are wye-connected.

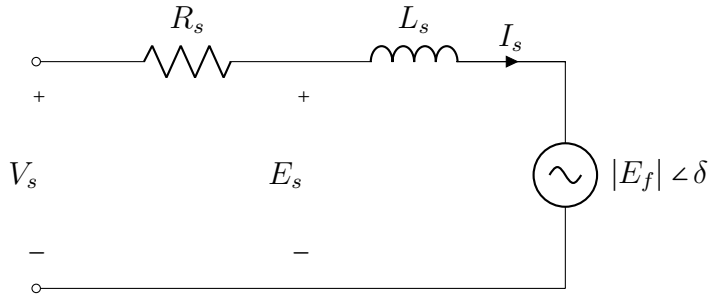

Figure 2.1: Machine Equivalent Circuit

In the circuit diagram in Figure 2.1, R_s and L_s are the stator resistance and inductance, respectively; V_s is the line-to-line input voltage with reference angle zero; I_s is the current vector through the winding; and E_f is the back emf voltage with δ as the phase shift. The electrical frequency, in rad/s, will be denoted as ω_e and the power factor angle is ϕ. From this circuit, the

current waveform can be realized as

$$I_s = \frac{V_s - (|E_f|\cos\delta + j\,|E_f|\sin\delta)}{R_s + j\omega_e L_s} \tag{2.1}$$

or in magnitude-angle form as

$$\begin{aligned} |I_s| &= \frac{\sqrt{(V_s - |E_f|\cos\delta)^2\,(|E_f|\sin\delta)^2}}{\sqrt{R_s^2 + \omega_e^2 L_s^2}} \\ \angle\phi &= -\arctan\frac{\omega_e L_s V_s + R_s\,|E_f|\sin\delta - \omega_e L_s\,|E_f|\cos\delta}{R_s V - R_s\,|E_f|\cos\delta - \omega_e L_s\,|E_f|\sin\delta}. \end{aligned} \tag{2.2}$$

As described in Equation (8) of [7], the maximum torque per ampere of stator current occurs when δ is maximized, denoted as δ_{max}, which can be solved through iterative solution schemes on the equation shown in Equation (2.3).

$$\omega_e L_s V_s \cos\delta_{max} = \omega_e L_s E_f + R_s V_s \sin\delta_{max}. \tag{2.3}$$

The desired control parameter is the voltage, so the phasor diagram for the circuit shown in Figure 2.1 is drawn to obtain an expression for V_s; the phasor diagram is shown in Figure 2.2. The resulting expression is determined to be

$$V_s = |I_s|\,R_s\cos\phi + \sqrt{|E_s|^2 - (|I_s|\,R_s\sin\phi)}. \tag{2.4}$$

In most instances, the small stator resistance encourages the approximation $R_s \approx 0$ reducing Equation (2.4) to $V_s \approx |E_s|$, where the expression for $|E_s|$ can be replaced with the volts per hertz constant, $K = \frac{V_{fr}}{\omega_{e,fr}}$, with fr indicating a system value observed at synchronous speed. The approximation produces a

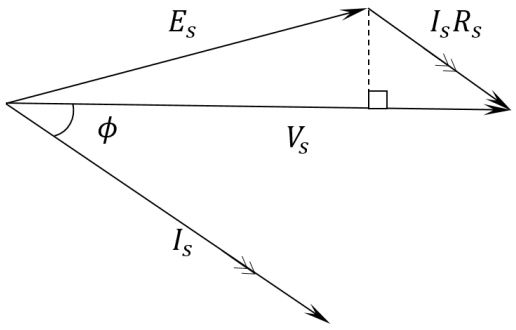

Figure 2.2: Vector Diagram for Voltage Equation

reduced equation for the voltage as a function of only the electrical frequency written as

$$V_s \approx |E_s| = K\omega_e = \frac{V_{fr}}{\omega_{e,fr}}\omega_e. \tag{2.5}$$

With the motor parameters and equations from [7], here represented as Equations (2.3) and (2.4), the authors were able to produce a volts per hertz nonlinear model for their machine, shown in Figure 7 of [7], which looks quite similar to that for the NASA PMSM in Figure 3.3. In the study, it was found that there was a voltage offset at zero electrical frequency that eventually converges to the presented linear equation in Equation (2.5) as the electrical frequency increases. The phenomenon of an offset voltage at low frequencies is a known problem for volts per hertz control systems caused by system characteristics, such as gate activation voltages and system losses, that commonly requires an alternative start-up method for the low frequency region of operation. In [7], the solution presented by the authors was to use the nonlinear model, shown in Equation (2.4) for open loop control. It should be noted that in many instances, PMSMs can be run open-loop with a volts per hertz controller to govern the system, particularly for high speed machines, as in [7] and [8]. Feedforward control can also be implemented into the system to obtain better performance as in [5], and feedback methods have also been attempted successfully as discussed conceptually in [9] and proven experimentally in [6]. Other sources have taken other approaches; for instance, to compensate for this effect and to obtain a more accurate representation of the full volts per hertz curve, a linear offset will often be added to the curve giving a better representation of low speeds and start up, as described in [9].

The task then becomes designing a sufficient control for this application based upon current knowledge of scalar control applications. While simple to implement, open-loop operation is not a feasible alternative because machine performance feedback provides critical information in aircraft applications, unlike in simple fan or pump systems in which this method is most commonly found. The need for a comprehensive understanding of system performance motivates a feedback based controller design. The feedback control presented in this work will be a speed feedback control and implement aspects of the architecture discussed in [9]. Speed feedback is used in this study because a dynamometer is anticipated to provide speed information during initial

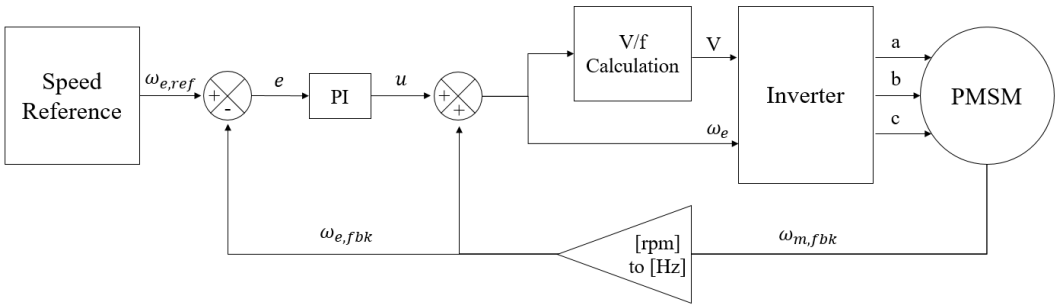

Figure 2.3: Volts/Hertz Controller with PI Speed Feedback Control

tests. However, speed feedback will eventually be estimated as has been recommended in previous literary works to create a sensorless control system, which is less prone to error [6], [10].

A simplified version of the control discussed in [9] can be seen in Figure 2.3. Control equations for volts per hertz control are based on the error, e, and control effort, u, as is typical of PID controllers, which can be represented by the equations

$$e(t) = \omega_{e,ref}(t) - \omega_{e,fbk}(t) \tag{2.6}$$

$$u(t) = K_p e(t) + K_i \int_0^t e(\tau) d\tau \tag{2.7}$$

with ref indicating the reference and fbk indicating feedback. Additionally, K_p and K_i are scalar proportional and integral control gains. The control effort, u, is then added to the measured feedback speed to output the line to line voltage, V, and electrical frequency, ω_e. The voltage equation contained within the V/f calculation block was expressed previously in Equation (2.5), and the equation for the electrical frequency is given as

$$\omega_e = u(t) + \omega_{e,fbk}. \tag{2.8}$$

At this point, it is important to recall that some models do not directly use the volts per hertz equation given in Equation (2.5), as was demonstrated in [7], or that another module may need to be added to the system in order to correct for lower frequencies, as is custom for boost voltage corrective schemes.

CHAPTER 3

MODELING MOTOR DYNAMICS AND IMPLEMENTATION OF A VOLTS PER HERTZ CONTROLLER

3.1 Analysis of the Volts per Hertz Curve

In order for the volts per hertz scalar control model to control the NASA PMSM, a knowledge of the PMSM's parameters is required; these values can be found in Table 3.1. The values shown in this table are the result of research conducted by the team, are used by all team members for numerical studies, and will be used for all empirical calculations throughout the document, unless otherwise specified.

Table 3.1: Motor Parameters for NASA PMSM

Motor Parameter	**Symbol**	**Value**	**Units**
Rated Power	P	1	MW
Rated Speed	$\omega_{m,fr}$	14,000	rpm
Rated Voltage	V_{fr}	675	$\mathrm{V}_{\ell\ell,\mathrm{rms}}$
Number of Poles	p	10	pole pairs
Stator Resistance	R_s	1.96	$\mathrm{m}\Omega$
Stator Inductance	L_s	1.65	$\mu\mathrm{H}$
Permanent Magnet Flux Linkage	F	33.76	$\mathrm{mV\,s}$
Rotor Inertia	J	0.6627	$\mathrm{kg\,m^2}$
Back emf Constant	K	61.2339	$\mathrm{V}_{\ell\ell,\mathrm{pk}}/(\mathrm{rad/s})$
Viscous Damping	d	8.09	$\mathrm{mN\,m\,s}$
Torque Rating	τ_ℓ	600	$\mathrm{N\,m}$

To obtain the volts per hertz curve for the system, an iterative approach was taken in Matlab to generate a volts per hertz curve from Equations (2.3) and (2.4), shown in Figure 3.1. Notice that there are two lines represented in this figure – the volts per hertz linear model and the nonlinear model generated from the PMSM's equivalent circuit, which more accurately describes

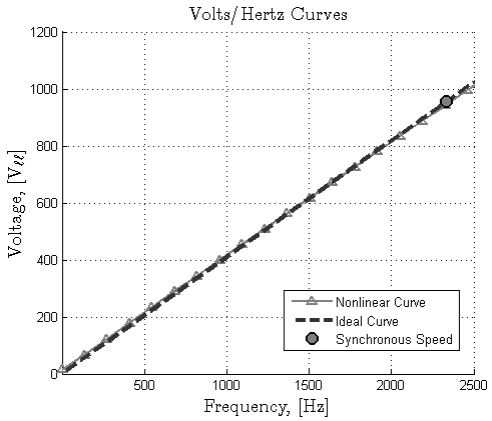

Figure 3.1: Volts per Hertz Curve for NASA PMSM

the system's dynamics. It is important to note that the nonlinear model is almost identical to the linear model. The correlation between linear and nonlinear models, expressed with the error to area ratio (E.A.R.), decreases with increasing frequency. The E.A.R. is expressed symbolically in Equation (3.1) and is additionally depicted in Figure 3.2 for the curves shown in Figure 3.1. Because the E.A.R. for high frequencies is low, it follows that the linear dynamic model expressed in Equation (2.5) can be used for control at higher mechanical speeds with the introduction of a corrective control, thus reducing the control model complexity. The curves for low frequency values, however, have higher E.A.R. values and will be more sensitive to changes in input voltage, requiring an alternative method of start-up for the system than the basic volts per hertz system dynamic curve.

$$\text{EAR} = \frac{\sum_i |x_{ref}(i) - x_{meas}(i)|}{\sum_i |x_{ref}(i)|}. \tag{3.1}$$

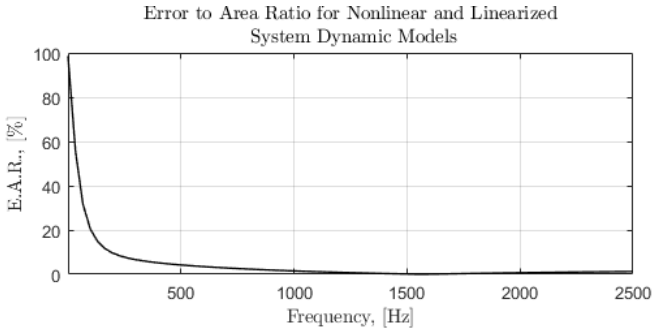

Figure 3.2: Error to Area Ratio (E.A.R.) for NASA PMSM

For low frequencies, an analysis of the effect of fluctuations in R_s on the ideal volts per hertz curve was performed, shown in Figure 3.3. This analysis was performed because R_s is exceptionally prone to variation in physical systems, particularly the stator resistance value increases a result of thermal variations [11]. It is shown that an increase in R_s corresponds to a larger E.A.R. for lower frequency values. For larger values of R_s, the system still converges to a value close to the linear model but requires higher frequencies for convergence to occur. Other system variables were additionally analyzed and the following trends hold true: with increased back emf constant, K, or increased stator inductance, L_s, E.A.R. for lower frequencies decreases.

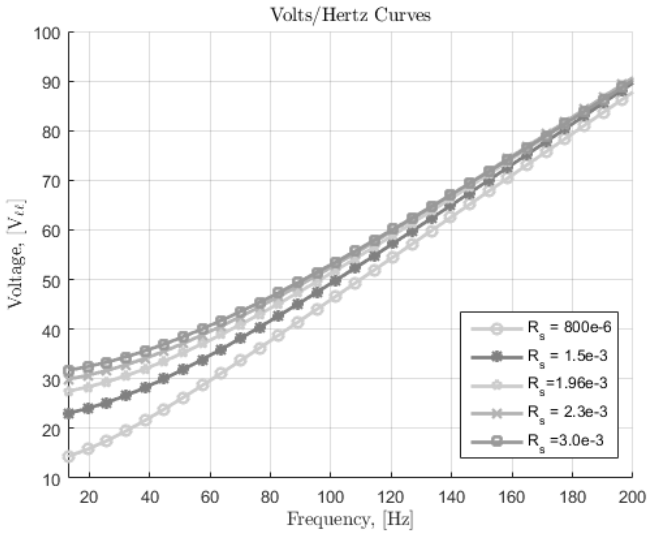

Figure 3.3: Volts per Hertz Curve Variation with Changes in R_s

As alluded to previously, there are two methods currently being explored in this work for correcting low frequency voltage offset: the addition of a boost voltage, which adds an offset to the machine's input voltage for low speeds, or implementation of the nonlinear model of the control system. Of the two, the former is preferred because the computation is substantially less complex; the boost voltage method reduces the number of feedback measurements and calculations that would need to be taken from the system. To explore the practicality of applying a boost voltage, a comparison of systems that have used volts per hertz control were analyzed; the relevant motor parameters came from sources [7], showing nonlinear control, and [5], showing standard volts per hertz control with corrective feedforward control; the values pre-

Table 3.2: Motor Parameters for Per Unit Comparisons

Parameter	Symbol	Units	NASA PMSM	Zhao et al. [7]					Itoh et al. [5]
				Motor 1	Motor 2	Motor 3	Motor 4	Motor 5	Motor 6
Voltage	V_s	V	675	100	50	380	360	28	155
Pole Pairs	p	poles	10	2	5	3	1	2	3
Mechanical Speed	ω_m	rpm	14,000	—	—	1,750	70,000	50,000	1,800
Electrical Speed	ω_e	Hz	2,333	—	—	58	2,333	1,667	90
Stator Inductance	L_s	H	1.65e-6	114.48e-3	6.93e-3	65.09e-3	39.60e-6	2.26e-6	16.06e-3
		p.u.	2.48e-3	86.4e-3	64.5e-3	35.6e-3	36.2e-3	10.7e-3	31.5e-3
Stator Resistance	R_s	Ω	1.96e-3	2.4	0.75	3.3	0.0055	0.06	0.348
		p.u.	2.09e-6	4.12e-3	596e-6	702e-6	26.1e-6	0.404e-6	1.45e-3

sented in these papers are shown in Table 3.2 as well as Figure 3.4. From a combination of these two sets of data, it is apparent that both the stator resistance and inductance are comparatively small for the NASA PMSM. As a small stator resistance can be attributed to a relatively linear volts per hertz curve, it can be naturally concluded that the stator inductance's small value is a predominant contributor to the distortion seen at smaller frequencies.

Looking at the motors depicted in Table 3.2 and Figure 3.4, it can be determined that low pole count is associated with a higher mechanical speed, N_m in rpm, despite comparable electrical frequencies, f_e in Hz, from

$$N_m = \frac{120}{2p} f_e. \tag{3.2}$$

For Motor 5, the decreased synchronous electrical frequency caused the operating range to be well within the nonlinear region, and the relatively low voltage caused increased relative error for the system forcing the use of the nonlinear dynamic model for system implementation. Because of the high pole count in the NASA PMSM, however, the synchronous speed is well within the linear region with minimal error. This indicates that, as the nonlinear region is relatively unobtrusive for standard operating speeds, it is unlikely that a full nonlinear model for the system dynamic will need to be implemented for the motor, and a boost voltage can be implemented for a controlled start-up of the system. This idea is reinforced by the data presented for Motor 6; even though the stator resistance was comparatively high, the larger voltage would reduce the E.A.R. for higher frequencies, similarly to the NASA PMSM, allowing the linear dynamic model to be used with some correction in feedforward control.

The NASA PMSM deviates from the linear model at low speeds as a result

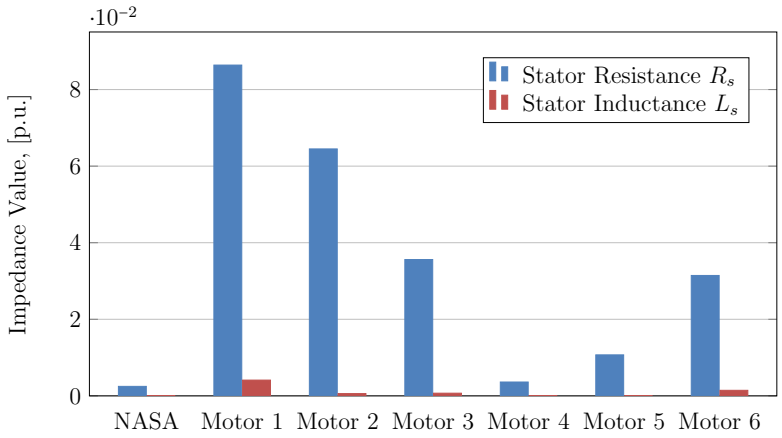

Figure 3.4: Stator Impedance Comparison for NASA PMSM and Various Motors Controlled with Volts per Hertz Control

of a low inductance value, and the non-linearity of this value is aggravated by increased stator resistance. However, because of the relatively high voltage of the system and high electrical frequency, this error is only relevant for lower frequencies, particularly below 500 Hz. The aforementioned will force the need of a corrective control for start-up of the system – the only time at which this motor will be operating at low speeds due to its use case. These observations will be important for the development of a start-up control for the system, particularly for physical implementation, and it is hypothesized that a boost voltage will be sufficient for the system. For physical implementation of the system, the low frequency operation will need to be studied further, considering sources of voltage loss in the motor and drive system that were not included in this analysis. However, the remainder of this thesis will be focused on the control design for maintaining and changing speeds close to the synchronous speed of 14,000 rpm.

3.2 Open Loop Dynamics of the Motor System

An open-loop speed reference, three phase signal generator, PWM gate signal generator, seven level FCML inverter, and the NASA PMSM were modeled in Simulink. A high-level block diagram of the Simulink model is shown in Figure 3.5. Of these modules, the three phase signal generator and motor model were Matlab generated subsystems, and the PWM generator and FCML inverter were created by another member of the research team. Thus,

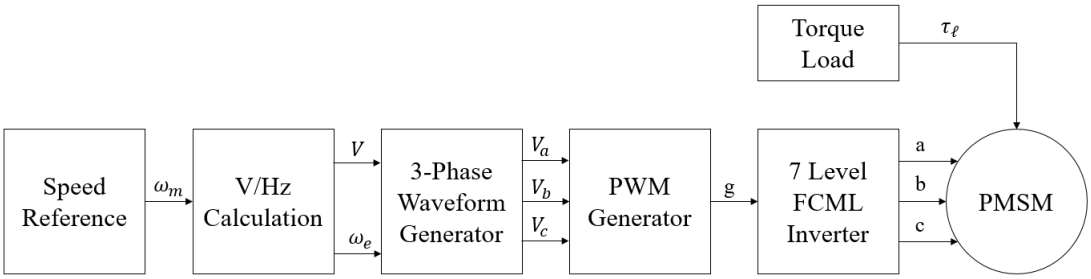

Figure 3.5: Open-Loop Volts per Hertz Curve for NASA PMSM

the focus of the simulation is on the speed controller design and integration. Results concluded from the simulation will focus on control around synchronous speed, being the most indicative of the operating characteristics of a propulsor during flight, with small but rapid variations from this value that are unique for an electric machine propulsion system.

For the initial test, the controller was held to a constant speed of 14,000 rpm under a torque load of 100 Nm. In order to avoid an instant loss of stability and deceleration to zero speed, the initial conditions for the motor at the starting point were determined; in particular, the starting angle of the rotor, θ_0, needs to align the winding field and permanent magnet field where θ_0 is limited to within 36 deg based on the number of pole pairs in the system. After multiple simulations, the controller did not generate a constant speed waveform for the synchronous speed but rather oscillated sinusoidally with increasing amplitude, see Figure 3.6.

The natural assumption as to the cause of the system characteristic observed in Figure 3.6 is that at the start of operation, the rotor's magnetic

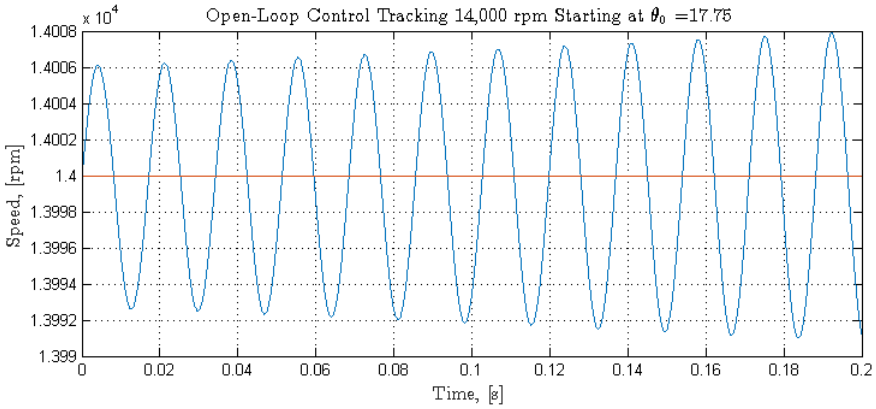

Figure 3.6: Constant Reference Speed Tracking with Open Loop Control

field was not properly aligned with the stator's magnetic field, thus causing amplified oscillations and making the system unstable; however, upon further inspection, the oscillations were found to be minimal with $\theta_0 = 17.25 \pm 0.25$ deg with the first oscillation peak at 14,006.104 rpm and the difference in amplitude between the first and second oscillation peaks at 0.122 rpm, as can be seen in Figure 3.7 comparing the peak oscillation speed to the difference between the first and second peaks. It was concluded that oscillations could not be eliminated from the open-loop control, though they could be mitigated by calibrating θ_0. Though the increase in amplitude between successive peaks is small, it will become significant for long run times and potentially cause the machine to lose stability.

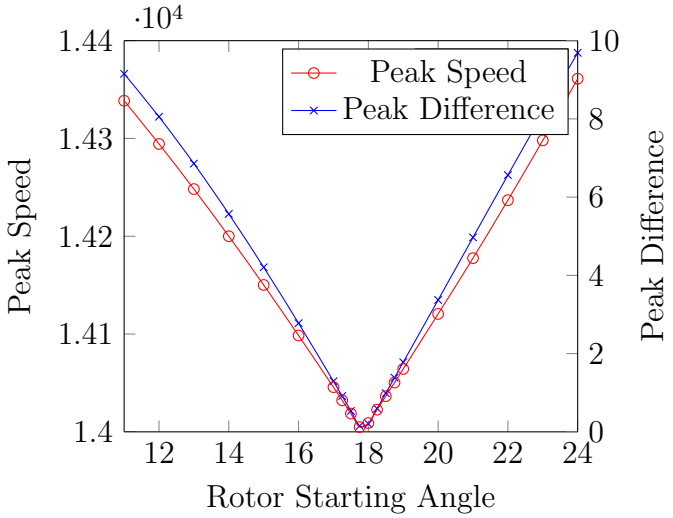

Figure 3.7: Mechanical Speed, ω_m [rpm], First Peak Oscillation Amplitude and Difference between Second and First Peaks versus Starting Rotor Angle, θ_0 [deg], for High Speed Start

Despite the oscillatory nature of the mechanical speed reference waveform, open-loop control will still track a continuous, periodic reference waveform, see Figure 3.8, where a sine wave centered at 14,000 rpm with amplitude of 1,000 rpm is tracked with open loop control. The oscillatory tracking verifies that the linear volts per hertz control model estimates the dynamics of the physical system but there is some inaccuracy in the model that will need correction for a completed, reliable controller. This correction can be accomplished through implementation of a closed-loop control model, discussed in Section 3.3.

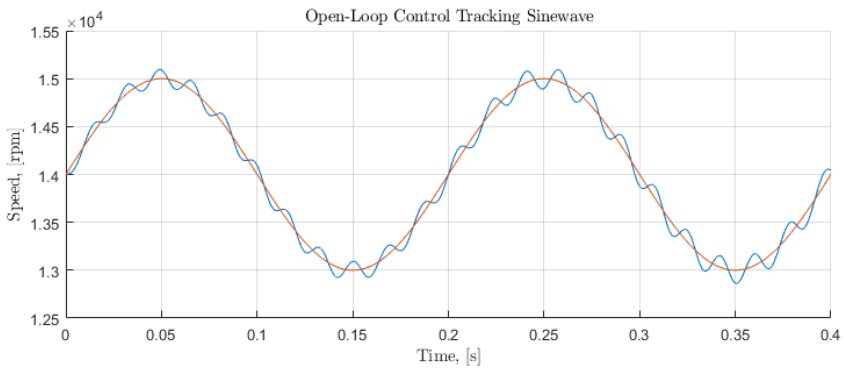

Figure 3.8: Sinusoidal Reference Speed Tracking with Open Loop Control Starting at Rotor Angle of 17.75 deg

3.3 NASA PMSM Volts per Hertz Controller Design

The standard closed loop control model for PMSMs using volts per hertz control is the PI controller. However, as the oscillations imply, the derivative term, associated with damping, is also needed in this particular case, differentiating the design from conventional controllers of this type. This idea was verified in simulation after observing that oscillations persisted for extensive combinations of proportional and integral gains. The derivative gain is most effective in situations where there is minimal, if any, noise. As a result, for a full system implemented in software/hardware, a filter is likely to be necessary on the speed feedback in order to mitigate aggressive response caused by the derivative gain against system noise. The derivative gain is also recommended to be a small value, particularly in comparison to the other controller gains, so that its effect is minimal and works to relieve small system oscillations rather than disrupt the system dynamic; this holds true for the simulated case where the derivative gain was 0.01 in comparison to a proportional gain of 10. Typically, the derivative gain is ignored because it is needed most often for minimization of overshoot in aggressive dynamic conditions, which can also be accomplished with a well tuned proportional and integral gain. Observations of plummeting rotor speed were also observed and corrected in [12], but the derivative gain proposed here is substantially more simplistic, resulting in a simple yet effective countermeasure.

In addition to concluding that the derivative gain was necessary for system stability, it was also found that the integral gain had nearly no effect on system stability, and in fact, could be attributed to worse dynamic response.

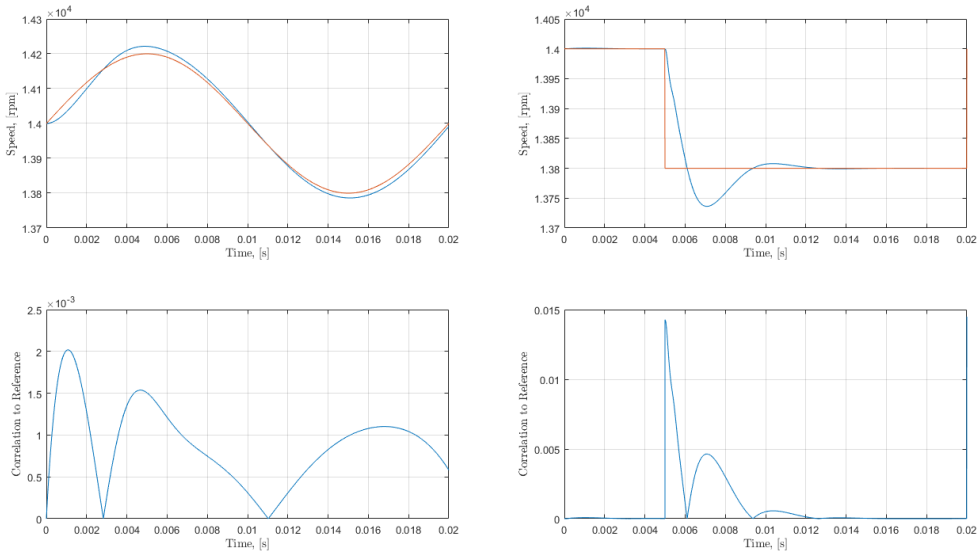

(a) Sinusoidal Reference

(b) Step Down Reference

Figure 3.9: Speed Waveforms with Best Correlation for Table 3.3 and Error to Area Plots for Gains $K_p = 10$, $K_i = 0$, and $K_d = 0.01$

Figure 3.9a shows a sinusoidal response and Figure 3.9b shows a step down response for the case that K_p is 10, K_i is 20, K_d is 0.01, and the load torque is held constant at 100 Nm. The waveforms shown in Figure 3.9 correspond to Table 3.3, showing the error to area ration for various K_i values with K_p and K_d held constant at 10 and 0.01, respectively. These tables indicate that the E.A.R. increases as K_i increases, reflecting an increase in the error with increased K_i. It is also observed that the K_i value that injects the least system error is zero. Thus, the integral gain was eliminated from the system

Table 3.3: Various Integral Gain Error Evaluation with Error to Area Ratio

Integral Gain, K_i	Sinusoidal E.A.R. [%]	Step Down E.A.R. [%]
0	0.0889490	0.0875566
1	0.0889491	0.0875604
5	0.0889693	0.0876251
10	0.0890101	0.0876767
15	0.0890268	0.0877108
20	0.0890576	0.0877575

as it did not assist in error correction. The combination of the integral term producing unsatisfactory results and the oscillations present in the open-loop system dynamic lead to the decision to alter the control architecture from that which is seen in Figure 2.3 to a PD controller in place of the PI controller. The equation specific to the PI control, Equation (2.7), becomes

$$u(t) = K_p e(t) + K_d \frac{de(t)}{dt} \tag{3.3}$$

representing the PD control effort with K_d representing the derivative gain. An updated block diagram can be seen in Figure 3.10.

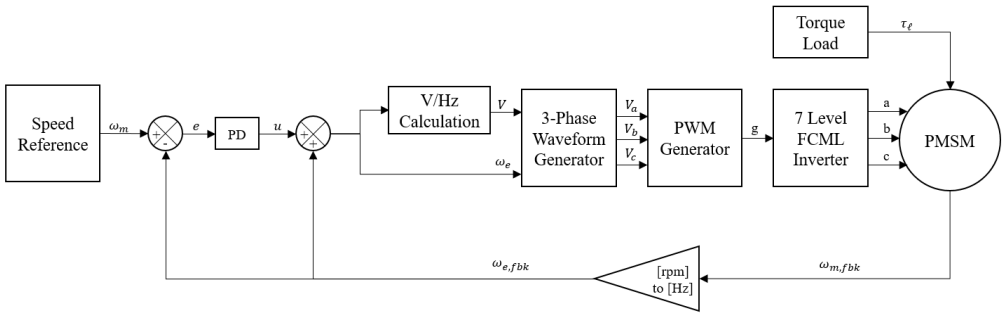

Figure 3.10: Closed-Loop Volts per Hertz Curve for NASA PMSM

The dynamic system response was studied for the PD control with K_p = 10 and K_d = 0.01 as the tuned, final proportional and derivative gains. A series of waveforms are shown in Figure 3.11 demonstrating the tracking capabilities of a constant 3.11a, sinusoidal 3.11b, triangular 3.11c, and step down 3.11d speed reference. The torque injection for each instance is shown in Figure 3.12; tracking persists despite large changes in torque added to the system. Though the torque step induced spikes in the constant speed tracking waveform shown in Figure 3.11a appear large, the impulses are roughly ±2 rpm, giving ±0.014 % error from the reference speed.

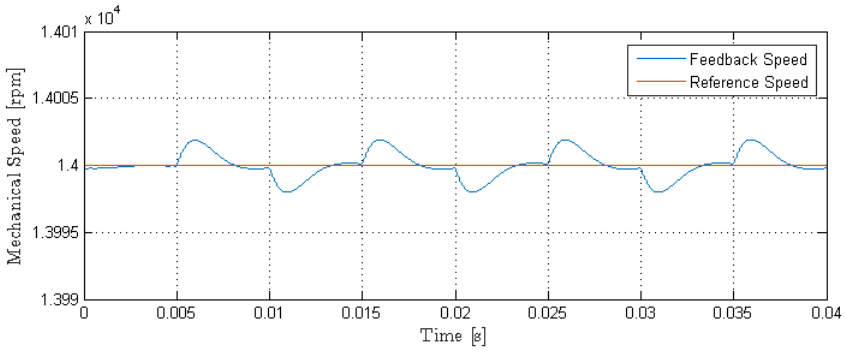

(a) Constant Reference

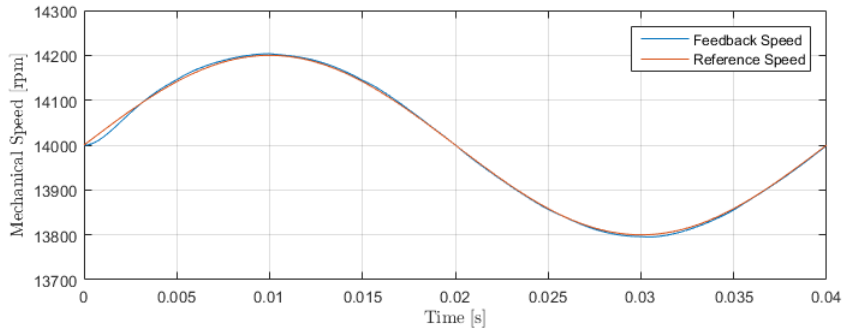

(b) Sinusoidal Reference

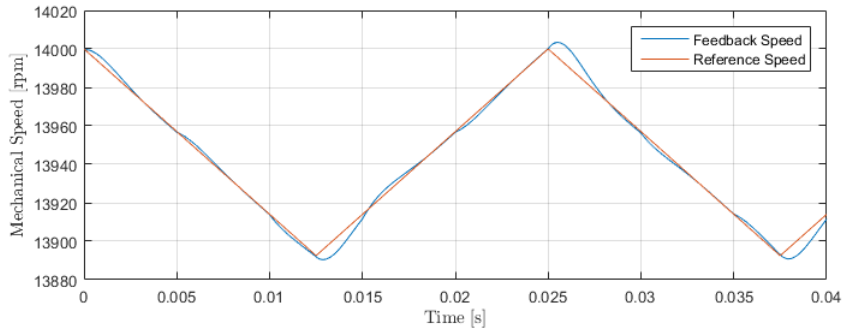

(c) Triangle Wave Reference

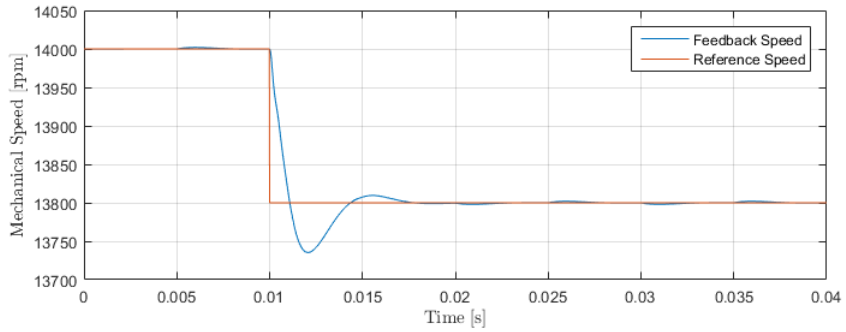

(d) Step Down Reference

Figure 3.11: Tracking Mechanical Speed Waveforms under Varied Torque Load Shown in Figure 3.12

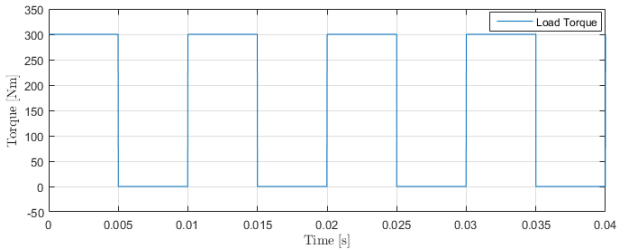

Figure 3.12: Torque Applied for All Waveforms Shown in Figure 3.11

Unfortunately, the PD control implementation was still found to have a failure mode: tracking for a large, instantaneous jump upwards in speed beyond 140±5 rpm. This phenomenon is apparent for both constant load torque of 100 Nm and the torque waveform shown in Figure 3.12. The issue is caused by mechanical speed feedback inaccurately representing the electrical speed feedback under large changes in speed. This problem is aggravated by the high speed and minimal radial spacing of different windings within the stator. Physically, when a large jump in reference speed is injected into the system control, the rotor's mechanical speed cannot keep up with the stator's electrical speed, the two lose synchronization, rendering the motor unstable, and the speed plummets to zero, shown in Figure 3.13. A sudden drop in reference speed had a similar tracking issue, but in this case, the loss of synchronous speed is corrected when the physical speed approaches the decreased reference speed and the system control begins to track the decreased reference signal, as is shown in Figure 3.11d. The corrective measure for the upward step causing loss of synchronous speed requires implementation of a softened, continuous change in the reference speed, which can be accomplished with a ramping function.

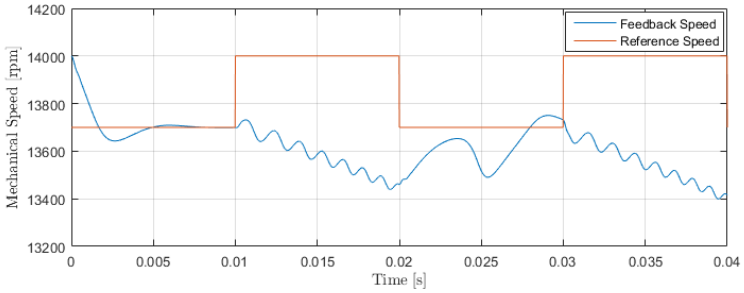

Figure 3.13: Torque Applied for All Waveforms Shown in Figure 3.11

3.4 Addition of a Ramping Function for Increased System Stability

The goal for the ramping function is to maximize the angular acceleration of the rotor in order to reach the reference speed in the minimal time possible without over-torqueing the motor. The relation of torque to acceleration is expressed as

$$\tau(t) = I\alpha(t). \tag{3.4}$$

In order to calculate the acceleration of the system, knowledge of the torque values is required. The ramping function should be designed keeping in consideration the maximum torque that could be output by the machine, τ_{max} = 600 Nm. Thus, calculating for the maximum possible acceleration manipulates the expression in Equation (3.4) to become

$$\alpha_{max}(t) = \frac{\tau_{max} - \tau(t)}{I} \tag{3.5}$$

where $\tau(t)$ expresses the instantaneous torque given by the motor. In order to find the instantaneous torque, an analysis of the total motor power consumption, $P_{3\phi}$, in relation to the torque was performed. The torque relates to $P_{3\phi}$ with the equation

$$P_{3\phi}(t) = \tau(t)\omega(t). \tag{3.6}$$

An expression for the instantaneous power can be calculated with the two watt-meter method, which is expressed as

$$P_{3\phi}(t) = V_{ab}(t)I_a(t) - V_{bc}(t)I_c(t). \tag{3.7}$$

By substitution of Equation (3.7) in to Equation (3.6) and solving for the torque results in the torque expression calculation

$$\tau(t) = \frac{V_{ab}(t)I_a(t) - V_{bc}(t)I_c(t)}{\omega(t)}. \tag{3.8}$$

Substitution of the torque equation represented in Equation (3.8) into the maximum acceleration function presented in Equation (3.5) and including the system feedback already provided for $[\omega_{fbk}]_{t_0}$ completes the expression

for the maximum angular acceleration.

To find an alternative expression for the ramping function that is smooth and maximizes acceleration towards the modified reference speed, the acceleration, $\alpha_{max}(t)$, shown in Equation (3.5), needs to be integrated to recover an expression for the instantaneous angular speed. As ramping will only be engaged once the reference and measured speed deviate by a specified error, there is an offset in time for the ramping function based on when it is determined there is sufficient error to require a ramp; this time will be denoted as t_0. Because the ramping function integration will not recover the initial offset of the speed, the speed feedback when a significant error is detected is added to the angular acceleration integration. The expression for the ramping function, or modified speed reference, can be expressed as

$$\omega_{ref}(t) = \int_{t_0}^{t} \alpha_{max}(t)dt + [\omega_{fbk}]_{t_0} = \omega(t) - \omega(t_0) + [\omega_{fbk}]_{t_0} . \tag{3.9}$$

For the application suggested in this work, the integral of Equation (3.5) can be calculated with a discrete integration block in Simulink, and the system conditions at the starting time for the ramp, t_0 (namely $\omega(t_0)$ and $[\omega_{fbk}]_{t_0}$), are recorded to calculate each successive value of $\omega_{ref}(t)$ until the reference tracks back to the reference speed and returns to the given reference speed value.

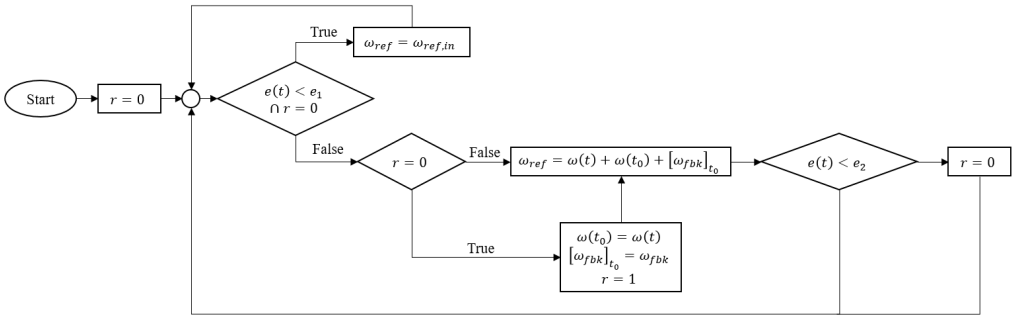

Figure 3.14: Software Flow for Ramping Reference Function

Implementing this approach requires software considerations for switching between passing the reference value and creation of a ramped reference function. The logical flow of this process can be seen in Figure 3.14. In the software flow model, there are two different error estimations: the error for the threshold in which to start the ramp, e_1, and the threshold in which

the ramp disengages, e_2. Additionally, because there is a threshold for the ramp to disengage such that there are no sharp overshoots, the two modes of operation, ramping ($r = 1$) and not ramping ($r = 0$), are specified.

To verify the ramping design, the torque estimation was examined as well as the complete system control. Starting with the torque estimation, after preliminary simulations, it was found that there was significant noise in the measurements injected by the PWM voltage levels generated by the FCML. The noise injected in the calculated torque feedback necessitated the use of a filter on the output of the torque calculation. The filter used was a simple single-pole, low-pass filter with a corner frequency of 50 kHz. The calculated torque versus measured feedback is shown in Figure 3.15; the load torque was given as a step function downwards, and the speed was maintained at 14,000 rpm.

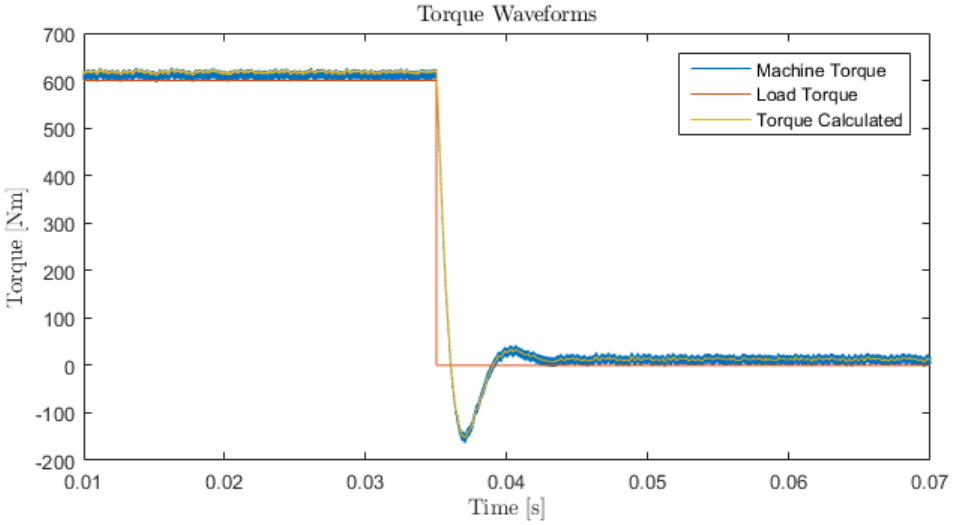

Figure 3.15: Torque Load, Machine Torque, and Filtered Torque Calculation for 14,000 rpm Speed Reference Waveform

The filtered torque, $\tau(t)$, was included in Equation (3.5) to obtain a function for the maximum angular acceleration of the rotor based on the remaining torque that the motor can apply. Using the Simulink discrete integrator block to evaluate $\alpha_{max}(t)$ and the process described in Figure 3.14 creates the system ramping function

$$\omega_{ref}(t) = \begin{cases} \omega_{ref,in} & |e(t)| < e_1 \ \cap \ r = 0 \\ \omega(t) - \omega(t_0) + [\omega_{fbk}]_{t_0} & \text{otherwise} \end{cases}. \tag{3.10}$$

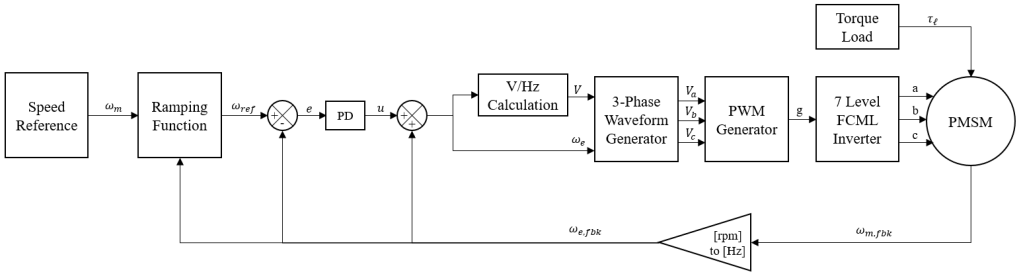

Figure 3.16: Closed Loop Control with Ramping Function

The final system controller model can be seen in Figure 3.16. Calculations of $\tau(t)$, $\alpha_{max}(t)$, and $\omega(t)$ are contained within the ramping function module. The dynamic performance for the ramping function was verified through testing of multiple waveforms with discontinuities; the waveforms can be seen in Figure 3.17 and Figure 3.18. In both of the aforementioned waveforms, ramping engages for a large change in speed until the system approaches the defined reference speed at which the ramp is disengaged and tracking continues for the given reference speed. In both figures, the load torque jumps downward for deceleration and upwards for acceleration. Additionally, the torque does not pass the threshold of 600 Nm in either case, so over-torqueing for the motor is avoided with the system ramping acceleration limit. It is thus verified that implementation of a ramping function to avoid discontinuities successfully corrects tracking failure associated with large jumps upwards in reference speed; ramping also can be used to prevent over-torqueing the machine during aggressive transitions.

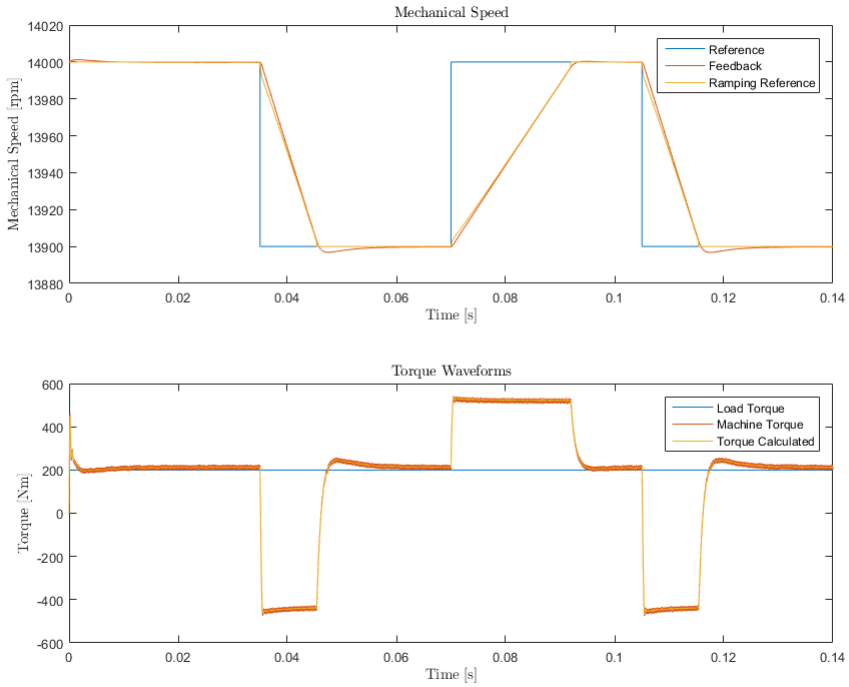

Figure 3.17: Tracking a Step Down and Up in Speed under Constant Torque Load

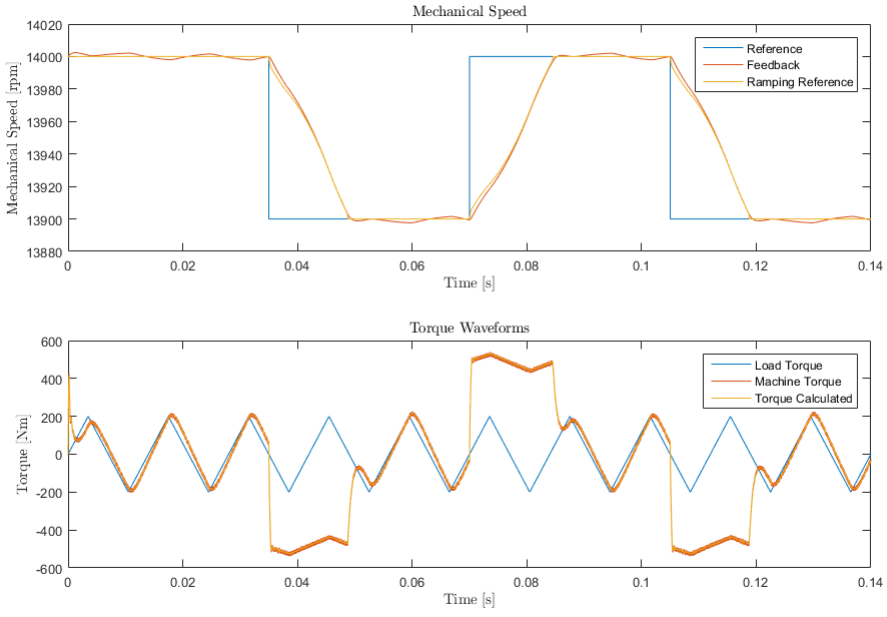

Figure 3.18: Tracking a Step Down and Up in Speed under Triangular Torque Load

CHAPTER 4

ANALYSIS OF VOLTS PER HERTZ CONTROL AS GOVERNING CONTROLLER

4.1 Analysis of Power in the Volts per Hertz System

The maximum system phase current is 1,000 A_{rms}, or 1,414 A peak, and the dc bus voltage is 1,000 V_{dc}. Power capacity for the system is 1 MW. To ensure that an overcurrent situation does not occur at full speed, full torque load, a simulation was run to verify the output of the inverter and motor. Torque load for the system was 600 Nm, and the speed was 14,000 rpm. The torque waveform measured from the machine can be seen in Figure 4.1; in this waveform, there is a roughly 15 Nm offset from the target. The offset is caused by friction and windage mechanical losses. The reference and mechanical speed waveforms can be seen in Figure 4.2, which shows the mechanical speed tracking the reference speed. Figures 4.3 and 4.4 show the three-phase current waveforms and the peak phase current, respectively. These figures indicate that the peak current is below the critical value for the static case. The voltage waveform from the inverter is shown in Figure 4.5; the voltage level for the highest inverter level is 1,000 V_{dc} where the control voltage is encoded within the PWM signal. Additionally, the mechanical power remains below 1 MW during the entire operation as can be seen in Figure 4.6. The high-frequency oscillations in some of the waveforms are a result of the switching of the FCML inverters. Though the electrical frequency is 2.33 kHz for a speed of 14,000 rpm, the switching frequency of the inverter is 120 kHz, which causes oscillations in data measurements, such as torque, current peak, and power waveforms. These oscillations are mitigated in analysis by considering the rms value of the waveforms. As a result of simulation and analysis of the resulting waveforms, it can be concluded that the volts per hertz control meets the needed specifications for the NASA PMSM for maximum loading conditions.

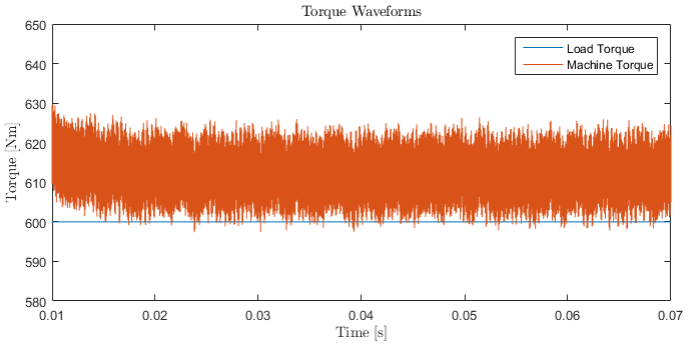

Figure 4.1: Mechanical Torque and Loaded Torque for Mechanical Reference Speed 14,000 rpm

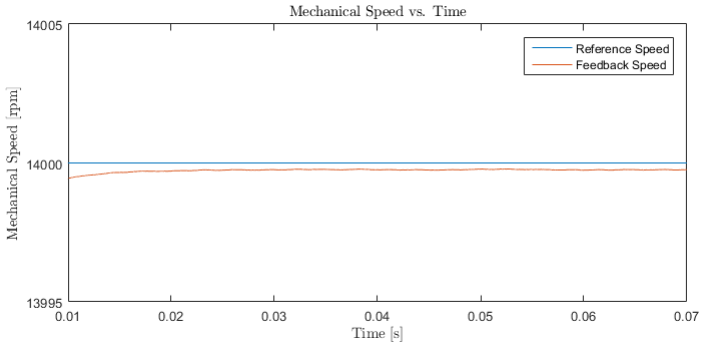

Figure 4.2: Reference Speed of 14,000 rpm and Measured Motor Speed

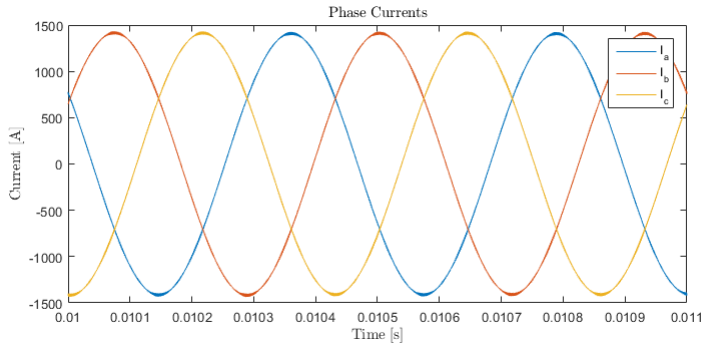

Figure 4.3: Current Waveforms I_a, I_b, and I_c out of FCML Inverter

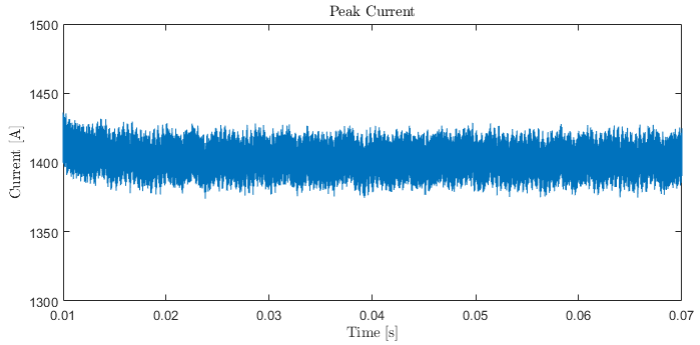

Figure 4.4: Peak Phase Current

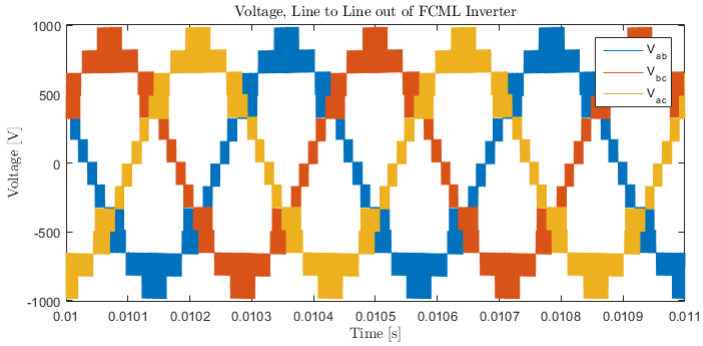

Figure 4.5: Line to Line Voltage of FCML Inverter for V_{ab}, V_{bc}, and V_{ac}

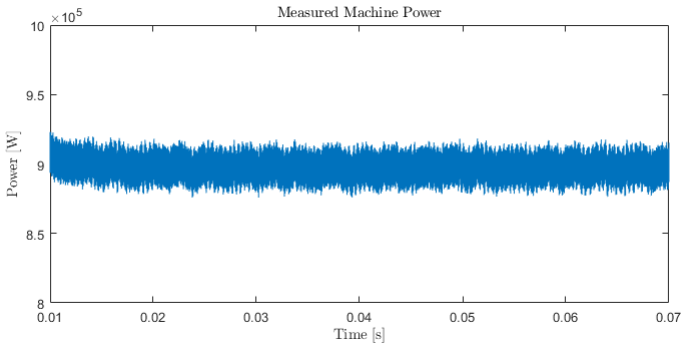

Figure 4.6: Power Measured for 14,000 rpm and 600 Nm

Once a control is implemented to track any given speed, the volts per hertz constant obtains some flexibility in value. Increasing the volts per hertz constant tends to decrease the peak current. The 1 MW power can be reached without overcurrent at 15,000 rpm and 600 Nm of torque load for a synchronous voltage of 790 V_{rms}. However, this adjustments necessitates an increase in the dc voltage to 1,050 V_{dc}.

4.2 Comparison of Volts per Hertz Control to Field Oriented Control

Volts per hertz and FOC are both typically used in applications that vary from the NASA PMSM. The volts per hertz controller can be seen in Figure 3.16, and the FOC control can be seen in Figure 4.7. In application, FOC is most commonly used in high precision, relatively low speed applications because of the computational density of the Clarke transform, Park transform, and inverse Park transform as well as the rotor position feedback to determine the dq-axis orientation. FOC is computationally dense and prone to error at high speeds. Volts per hertz control is typically used for high speeds with constant load torque because the possibility of open-loop implementation and fast computation time prove advantageous. However, it does not regulate current or torque, creating failure modes for high power, particularly over-current and over-torque. To investigate which control scheme is better for the application, simulations were run for each with identical torque loading and reference speed.

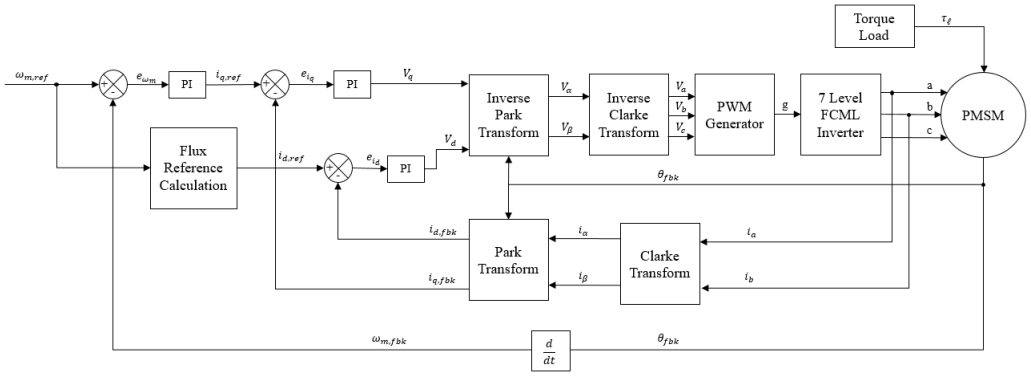

Figure 4.7: Field-Oriented Control Block Diagram

4.2.1 Dynamic Response

To analyze the dynamic response of the system, both the FOC and volts per hertz control were recorded with common load torques and reference speeds. Shown in Figure 4.8b and 4.8a is the speed response under varied torque load. For the FOC controller, the peak overshoot is 0.09 rpm and the peak undershoot is 5.82 rpm. The peak overshoot and undershoot for the volts per hertz controller are comparable at 3.33 rpm and 4.51 rpm, respectively. Steady state error is substantially more impactful in the FOC controller at 4.62 rpm at max. Steady state error for the FOC mechanical speed varied with the torque load. The steady state error for the volts per hertz control was 0.2 rpm.

Torque was also monitored in the field oriented and volts per hertz controllers. In both cases, the torque tracks the load torque and decreases drastically during deceleration. The minimum and maximum torque were -720 Nm and 590 Nm for FOC and -605 Nm and 610 Nm for V/f. For the torque limits, a discrepancy exists between the two models, namely, the saturation limit for the FOC torque was designed for 714.4 Nm instead of 600 Nm. A comparison of V/f and FOC torque characteristics can be seen in Figure 4.9a and Figure 4.9b. The FOC controls the torque with the torque current, i_q, PI controller while the V/f control limits the torque with the ramping function instead of a direct controller and otherwise compensates for load torque to maintain speed. Because the torque control is present in FOC making it possible to reach a controlled power maximum, the dynamic response for speed tracking is faster. This could be seen in Figure 4.8a and 4.8b where speed tracking of reference 14,000 rpm dropping to 13,500 rpm is 0.03 s for the FOC model and 0.037 s for the volts per hertz model. The variation in torque limits is a significant cause for the 0.007 s deviation in setting time between the controllers.

The current and power waveforms were also produced for the FOC and V/f control. Peak power was -1.05 MW and the peak current was 1,425 A for FOC as compared to 0.91 MW and 1,405 A for volts per hertz. Because the target ratings for both systems were varied there is no direct comparison for these metrics.

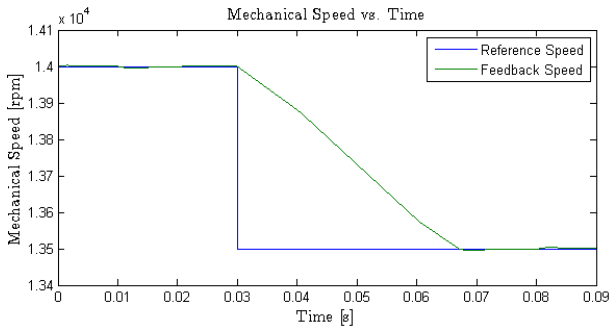

(a) V/f Speed Tracking

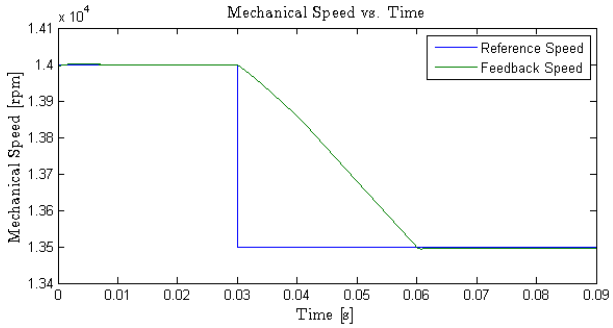

(b) FOC Speed Tracking

Figure 4.8: Reference Speed Tracking Comparison

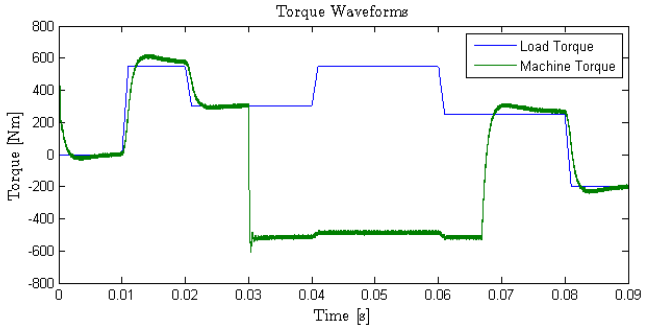

(a) V/f Torque Response

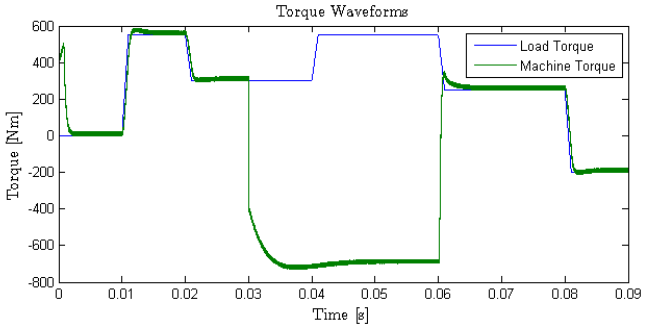

(b) FOC Torque Tracking

Figure 4.9: Torque Response Comparison

Integral Error in FOC Control

In the current model of FOC, the PI gains for the current control are K_p = 0.05, K_i = 20, and the PI gains for the speed control are K_p = 300, K_i = 500. Though not exclusively true, large gains can cause instability in PID control systems, particularly derivative and integral terms. Issues with the derivative term were addressed in Section 3.3. The integral control in the FOC method introduces additional concerns, namely integral windup. When there is consistent error in the system that is not corrected, error accumulates in the integral term over time. The influence of integral windup is delay in response or saturation of the control effort. Since a higher gain is associated with more aggressive response, the high integral gains are likely to aggravate integral windup and introduce a source of failure in the FOC model. Potential correction is activation of the integral gain only within limited error bounds; however, this method is not ideal because of the steady state error shown in the FOC controller.

4.2.2 Position Feedback

The main failure mode for FOC is associated with position error of the rotor. If measurements are not accurate, synchronous speed will be lost. In severe instances, inaccuracy in the position measurement can cause the speed to plummet to zero. A single revolution of the rotor occurs in 4.286 ms at 14,000 rpm. With 10 pole pairs, poles are placed every six degrees radially, giving a ±3 deg tolerance in the position measurement. This means that an accurate speed measurement must be sent to the controller at a maximum of every 71.4 μs to obtain a single position measurement for each of the windings. In practice, measurements need to be taken much more frequently to increase precision and compensate for noise in the system. Further constraint on the system is associated with calculation of the control effort between successive position samples; that is to say, all computation and communication, outlined in Figure 4.7, needs to be executed in less than 71.4 μs.

The rotor position can be obtained in two ways: absolute rotary encoder measurement and sensorless position estimation. For the first alternative – integration of a speed/position sensor into the system – noise is injected in the form of measurement error based on the resolution of the device and

measurement accuracy. Even for high-precision devices, high-speed encoders typically have short lifetimes because most optical solutions obtain contaminants over time and moving components wear out quickly [13]. Because of the physical disadvantages associated with a sensor, it is the general consensus in the literature that most high-speed machines move to sensorless operation. However, sensorless speed and position estimation necessitates an accurate representation of the motor impedance and flux linkage parameters or steady state error will occur. The rotor resistance and inductance values are temperature sensitive, so calculations will obtain error with variations in ambient temperature [14]. In particular, an increase in temperature will increase a machine's synchronous resistance [11]. Position estimation is a failure mode for the FOC design because of the high precision required to obtain an accurate estimate of the stator position from a machine with high pole count at high speeds.

In contrast, though there are more feedback measurements required for volts per hertz control, position feedback is eliminated and the data that is needed can be recorded at a much slower rate. For the power calculation, error is mitigated with a filter to remove noise. To synchronize data, data collection can be triggered on the same clock cycle for all feedback sensors minimizing delay error between successive measurements. Consequentially, timing constraints and small measurement errors are substantially less prone to causing system failure in volts per hertz control than the FOC.

4.2.3 Dynamics Limitations in Volts per Hertz Control

Though volts per hertz control was modified in this thesis to have a ramping function to transition between high reference speed steps and ramping is designed to have limits on the torque for high error transitions, it does not correct issues with over-torque and over-current, so lock rotor conditions and current surges are still a possibility in the system design. In order to correct the aforementioned issues, limits need to be applied directly to the control effort. As a result, if the volts per hertz controller is selected as the governing controller of the system, more research needs to be done in prevention of over-torque and over-current cases, which is still in progress.

4.2.4 Summary of Controller Characteristics

The comparison between the two controllers is summarized in Table 4.1. It was found that overshoot was comparable between controllers and steady state error was increased for FOC, which could cause a source of failure in the K_i gain called integral wind-up. More measurements are taken in V/f and care must be taken to record data points synchronously, but in FOC, the stator position estimation requires high rate computation and communication. Though the dynamic response appears to favor V/f, the system has a design flaw in being unable to limit current and torque to the system without additional conditioning on the control effort.

Table 4.1: Comparison of Volts per Hertz (V/f) and Field Oriented Control (FOC) Performance and Characteristics

	V/f	FOC
Feedback Signals	Mechanical speed (ω_m) Line to line voltages (V_{ab}, V_{bc}) Phase currents (I_a, I_c)	Mechanical speed (ω_m) Stator position (θ)
Failure Modes	Over-torque Over-current	Position error Computation time Integral wind-up
Steady State Error	0.2 rpm	4.62 rpm (load dependent)
Peak Overshoot	4.51 rpm	0.09 rpm
Peak Undershoot	3.33 rpm	5.82 rpm

In the case where load torque is unpredictable, FOC would be the preferred controller because the embedded saturation limits provide safety against over-current and over-torque. However, with predictable torque loading, as is often seen in fans and pumps, V/f is a less error prone option for the high speed application. As a result, more work will be done to find a way to adapt limits for failure modes.

CHAPTER 5

MODERN AIRCRAFT PROPULSORS AND INTEGRATION OF THE NASA PMSM

Modern commercial aircraft propulsion makes use of turbofan technology to generate thrust. A turbofan engine has a number of stages. The inlet fan forces air around the turbine and allows flow into the turbine core. The air flowing into the turbine core passes through a low pressure, then a high pressure compressor before moving into the combustion chamber. Fuel is combined with the air and combusted. Hot air is then forced out of the high pressure turbine and low pressure turbine, turning the shafts and generating thrust on the inlet fan. This architecture can be seen in Figure 5.1.

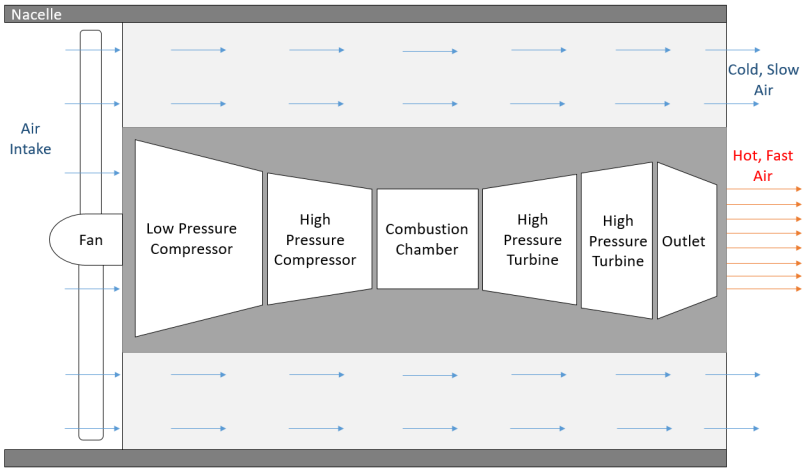

Figure 5.1: Diagram of Turbofan System

Green energy trends as well as the low efficiency of turbine machines are motivating changes in the current turbofan drive system. There are two strategies to develop an electric propulsion system: hybrid-electric turbine/motor systems and directly driving the inlet fan with an electric motor. For the hybrid-electric integration strategy, the main change from the turbofan strategy is that instead of using a starter motor to turn on the turbofan, the NASA PMSM is proposed to be used to turn on the turbofan and assist

in driving the turbofan shaft during flight. This approach has a mechanically similar design and has many of the same design challenges as a turbofan system, but with increased performance based upon the improved efficiency profile of the PMSM. The direct drive case, however, reduces the mechanical complexity.

5.1 Hybrid-Electric Technology

The NASA PMSM is proposed to be a highly efficient machine at 97.4% efficiency. In comparison, the highest efficiency gas turbine currently on the market, the H-class performance Siemens gas turbine SGT-8000H Series 275 MW machine, is only 40% efficient because of the extra overhead of driving compressors and windage losses [15]. In particular, the compressor speed and power consumption are maintained throughout operation regardless of mechanical output power to maintain consistent combustion chamber conditions. This causes the heat rate, or the fuel per output power relationship, to increase. The result is that operation at rated speed is the most efficient while low speeds see a dramatic decrease in efficiency. The system weights are also dramatically different at 65.4 kg for the NASA PMSM and 289 metric tons for the Siemens turbofan. Because of the high efficiency and low mass, the specific power for the PMSM is 15 kW/kg. In comparison, the Siemens turbine has only 1.02 kW/kg, and the GE90-115B turbofan has a specific power of 10 kW/kg [15], [16]. The specific power and efficiency may be higher for the NASA PMSM, but the low energy density of battery technology has kept turbofans in use. However, because of the high specific power of the NASA PMSM, it is still anticipated to improve system efficiency in hybrid-electric implementation.

In integration of a hybrid-electric drive, failure modes for the turbofan and PMSM need to be considered because they are both present. Discussion of the failure modes for the PMSM have largely been covered in Chapter 4. Introduction of the turbofan adds the possibility of surge, over-temperature, over-speed, over-pressure, and blowout failure modes [17]. As a result of the turbofan failure modes, the Federal Aviation Administration (FAA) has placed regulations on turbofan dynamic performance to prevent compressor surge and blowout [18]. For a throttle change from 100% to 40%, 1.63 s was

the minimum observed settling time in experimentation in [19]. As compared the NASA PMSM, the minimum response time estimated was 0.6 s. This shows that the NASA PMSM has a faster response than the turbofan for both proposed control schemes, so control will need to be limited to comply with FAA regulation [19].

5.2 Direct Drive Technology

Direct drive propulsion systems for aircraft are a hypothesized electric implementation to replace turbofan technology. Implementation of a direct drive system is a far-reaching goal as energy density in fuel cells is not yet competitive with A-1 jet fuel.

It is hypothesized that the lower inertial system could increase dynamic performance in speed and torque. Limits based upon compressor surge and blowout can be eliminated from the system because they are not present when the gas turbine is removed. Fan inertia still needs to be considered. If dynamic speed and torque are increased with the application of an electric propulsion system, wear on the fan blades is the next point of fatigue. As such, if performance specifications are increased to enable the improved dynamic performance of the electric propulsion system, further research should be performed into the acceleration limits that maximize fan lifetime and prevent other sources of aerodynamic stall. Direct drive also has the benefit of mechanical simplicity, low weight, and increased serviceability with the removal of the turbine.

Recovery from a PMSM failure is simpler than recovery from turbine failure. The most common PMSM failure mode is loss of synchronization. In the case that synchronization is lost, stopping and attempting to restart the PMSM should restore stability. Correction for the turbine failure is also a restart attempt, but it requires a large, instantaneous power consumption by the turbine's starter motor to get the turbine back to rated speed. The gas turbine also has the potentially non-recoverable failure of back-surge, which is known to destroy turbines in extreme instances. The parallel to surge in the PMSM is over-torque and over-current. Torque is estimated in both the V/f and FOC models to minimize the risk of failure. Additionally, current can be read from the system and control can be implemented to prevent

over-current failure as well. Another feature present in the electronic drive system not present in the turbofan design is the ease of feedback information. In the typical turbofan application, the primary feedback variable is fuel flow rate because other metrics, such as thrust, cannot be directly measured [17]. However, because of the electrical elements present in the PMSM drive system, access to monitoring electrical variables and performing calculations to obtain additional motor performance metrics is much more available.

CHAPTER 6

CONCLUSION

The objective of this thesis was to design a control system for the NASA PMSM with integration of FCML inverter, compare the control design with other control strategies, and compare to current dynamic models used in commercial aircraft. The volts per hertz model was designed, linearized, implemented in control, and tested on a nonlinear model. The system controller was a PD controller to remove oscillations, and a ramping function was added to keep machine and electrical speeds aligned for feedback. The controller was found to meet power specifications for 14,000 rpm. The volts per hertz controller was then compared to the FOC control design, and it was determined that the designs were comparable with differing failure modes in each controller. The volts per hertz controller needs additional limits for over-torque and over-current analysis, while the FOC controller has to handle volatile variable feedback at high speed with the risk of windup error from the high integral gain. In comparison to modern propulsion systems, both the FOC and V/f control offer faster dynamic response; thus, either must be limited to meet FAA regulations. The control design for both systems offers more easily accessible feedback data, and the integration of a direct drive electric motor propulsion system can eliminate some traditional failure modes seen in turbofan applications.

Further work in development of the volts per hertz control is expanding the methodology for the ramping function to create a general limiting algorithm for the load torque. Additionally, formulation of an over-current strategy needs further research. As the torque can be calculated and current can be monitored with feedback, devising a protection methodology is thought to be possible. Additional tests can be implemented to determine controller robustness. Research on the implications of hybrid-electric and direct drive electric technology will also be explored with continued advancement towards hybrid-electric and electric aircraft propulsion technology.

REFERENCES

[1] Y. Lei, W. C. Liu, and R. C. N. Pilawa-Podgurski, "An analytical method to evaluate flying capacitor multilevel converters and hybrid switched-capacitor converters for large voltage conversion ratios," in *2015 IEEE 16th Workshop on Control and Modeling for Power Electronics (COMPEL)*, July 2015, pp. 1–7.

[2] X. Yi, "Electromahnetic-thermal modeling for high-frequency air-core permanent magnet motor of aircraft application," M.S. thesis, University of Illinois at Urbana-Champaign, 2016.

[3] D. A. Torrey, *AC Electric Machines and Their Control*. E-Man Press LLC, 2011.

[4] M. Marufuzzaman, M. B. I. Reaz, L. F. Rahman, and T. G. Chang, "High-speed current dq PI controller for vector controlled PMSM drive," *The Scientific World Journal*, vol. 2014, no. 709635, pp. 1–9, January 2014.

[5] J. I. Itoh, N. Nomura, and H. Ohsawa, "A comparison between V/f control and position-sensorless vector control for the permanent magnet synchronous motor," in *Proceedings of the Power Conversion Conference-Osaka 2002 (Cat. No.02TH8579)*, vol. 3, 2002, pp. 1310–1315.

[6] G. D. Andreescu, C. E. Coman, A. Moldovan, and I. Boldea, "Stable V/f control system with unity power factor for PMSM drives," in *2012 13th International Conference on Optimization of Electrical and Electronic Equipment (OPTIM)*, May 2012, pp. 432–438.

[7] L. Zhao, C. H. Ham, Q. Han, T. X. Wu, L. Zheng, K. B. Sundaram, J. Kapat, and L. Chow, "Design of optimal digital controller for stable super-high-speed permanent-magnet synchronous motor," *IEE Proceedings - Electric Power Applications*, vol. 153, no. 2, pp. 213–218, March 2006.

[8] L. Zhao, H. Chan, and T. Wu, "A new design approach of an ultra high-speed permanent magnet synchronous motor (PMSM) system," in *INTERMAG 2006 - IEEE International Magnetics Conference*, May 2006, pp. 306–306.

[9] B. K. Bose, *Modern Power Electronics and AC Drives*. Prentice Hall PTR, 2002.

[10] B. H. Bae, S. K. Sul, J. H. Kwon, and J. S. Byeon, "Implementation of sensorless vector control for super-high-speed PMSM of turbocompressor," *IEEE Transactions on Industry Applications*, vol. 39, no. 3, pp. 811–818, May 2003.

[11] D. Montone, *Temerature Effects on Motor Performance*, Haydon Kerk Motion Solutions / Pittman Motors, 2013.

[12] D. Montesinos-Miracle, P. C. Perera, S. Galceran-Arellano, and F. Blaabjerg, "Sensorless V/f control of permanent magnet synchronous motors," *Motion Control*, pp. 439–458, 2010.

[13] Y. Zhao, "Position/speed sensorless control for permanent-magnet synchronous machines," Ph.D. dissertation, University of Nebraska, 2014.

[14] *Digital Motor Control Software Library: Target Independent Math Blocks*, Texas Instruments, Inc., 2013.

[15] *SGT-8000H Gas Turbine Series - Proven in Commercial Operations*, Siemens, 2015.

[16] "The GE90 engine," 2017, General Electric Corporation. [Online]. Available: http://www.geaviation.com/commercial/engines/ge90-engine

[17] S. Garg, "Fundamentals of aircraft turbine engine control," 2012, National Aeronautics and Space Administration (NASA) Glenn Research Center Controls and Dynamics Branch. [Online]. Available: https://www.grc.nasa.gov/www/cdtb/aboutus/Fundamentals_of_Engine_Control.pdf

[18] *Federal Aviation Regulations/Aeronautical Information Manual 2013*, Federal Aviation Administration (FAA), 2013.

[19] J. S. Litt, D. K. Frederick, and T. Guo, "The case for intelligent propulsion control for fast engine response," National Aeronautics and Space Administration (NASA) and the American Institute of Aeronautics and Astronautics (AIAA), Tech. Rep. 2009-215668, November 2009.